Integral Equation Methods for the Morse-Ingard Equations

Xiaoyu Wei[a], Andreas Klöckner[a,*], Robert C. Kirby[b]

[a] *Department of Computer Science, University of Illinois at Urbana-Champaign, Champaign, Illinois, United States*
[b] *Department of Mathematics, Baylor University, Waco, Texas, United States*

Abstract

We present two (a decoupled and a coupled) integral-equation-based methods for the Morse-Ingard equations subject to Neumann boundary conditions on the exterior domain. Both methods are based on second-kind integral equation (SKIE) formulations. The coupled method is well-conditioned and can achieve high accuracy. The decoupled method has lower computational cost and more flexibility in dealing with the boundary layer; however, it is prone to the ill-conditioning of the decoupling transform and cannot achieve as high accuracy as the coupled method. We show numerical examples using a Nyström method based on quadrature-by-expansion (QBX) with fast-multipole acceleration. We demonstrate the accuracy and efficiency of the solvers in both two and three dimensions with complex geometry.

Keywords: The Morse-Ingard Equations, Fast Multipole Method, Integral Equation Method, Quadrature-by-Expansion

---

1. Introduction

The Morse-Ingard equations are time-harmonic, steady-state equations derived from the linearized Navier-Stokes equations [4, 12]. They model the pressure and the temperature variations of a fluid due to a heat source inside the fluid, in a regime where both the acoustic wavelength and the thermal boundary layer thickness are of interest. Specifically, we consider the following nondimensionalized Morse-Ingard equations from [4]: in the

---

[*] Corresponding author

Email addresses: `xywei@illinois.edu` (Xiaoyu Wei), `andreask@illinois.edu` (Andreas Klöckner), `Robert_Kirby@baylor.edu` (Robert C. Kirby)

fluid domain D^c with $D \subset \mathbb{R}^d$ bounded,

$$\begin{cases} \Omega\nabla^2 T + iT - i\dfrac{\gamma-1}{\gamma}P = S, \\ (1-i\gamma\Lambda)\nabla^2 P + \left[\gamma\left(1-\dfrac{\Lambda}{\Omega}\right)+\dfrac{\Lambda}{\Omega}\right]P - \gamma\left(1-\dfrac{\Lambda}{\Omega}\right)T = -i\gamma\dfrac{\Lambda}{\Omega}S, \end{cases} \tag{1}$$

where P is the pressure field, T is the temperature field, S is the heat source, and Ω, Λ, γ are dimensionless parameters.

The application that motivated this work is to model trace gas sensors that utilize optothermal and photoacoustic and effects to aid designing such sensors. The **q**uartz-**e**nhanced **p**hoto**a**coustic **s**pectroscopy (QEPAS) sensor, for example, employs a quartz tuning fork to detect via the piezoelectric effect the acoustic pressure waves that are generated when optical radiation from a laser is periodically absorbed by molecules of a trace gas [6, 8]. The **r**esonant **o**pto**t**hermo**a**coustic **de**tection (ROTADE) sensor, on the other hand, uses the same tuning fork to detect the thermal diffusion wave via the indirect pyroelectric effect [7]. An efficient and accurate solver for the Morse-Ingard equations on the exterior domain can be a key tool for the modeling and design of both QEPAS and ROTADE sensors [4, 14, 17].

To suit this application, we consider the thermoacoustic scattering problem, where the *scattered waves* obey the homogeneous Morse-Ingard equations on the exterior domain ($S = 0$), coupled with sound-hard boundary conditions in pressure and continuity in heat flux, leading to Neumann boundary conditions in both T and P,

$$\begin{cases} \left.\dfrac{\partial T}{\partial n}\right|_{\partial D} = g_T, \\ \left.\dfrac{\partial P}{\partial n}\right|_{\partial D} = g_P, \end{cases} \tag{2}$$

where the volumetric source S in (1) is accounted for by the *incoming waves* it induces in the boundary conditions above.

For solution uniqueness, we also require

$$T(x) < \infty \text{ and } P(x) < \infty, \quad \text{when } |x| \to \infty. \tag{3}$$

As shown in [17], (3) ensures solution uniqueness by ruling out unphysical waves from the infinity, similar to what the Sommerfeld radiation condition does for the Helmholtz equation. In our applications, the wave number has positive imaginary part. Therefore, boundedness at infinity is sufficient. For general wave numbers, we also provide a direct generalization of the Sommerfeld condition in Section 2.3.

In this paper, we propose two integral-equation-based methods for (1) to (3). For both methods, we derive representations of the solution in terms of layer potentials involving unknown densities, leading to integral equations that can be reduced to the form of a Fredholm integral equation of the second kind

$$(I - A)\rho = f, \tag{4}$$

where A is a compact integral operator; therefore, our methods are all based on second-kind integral equation (SKIE) formulations. SKIEs are attractive because both the condition number and the number of iterations required for iterative solvers like GMRES [16] are bounded by constant when refining the mesh. In fact, [11] gives rigorous superlineary GMRES convergence estimates in this case. The first method is based on a direct SKIE formulation to the original equations using the free-space Green's functions. While deriving the analytic formula for the free-space Green's functions, we also obtain a decoupling transform that converts the problem into two decoupled Helmholtz equations, with decoupled Neumann data. Our second method takes advantage of this transform and uses SKIEs for the Helmholtz equations to obtain the solution. As such we refer to the first method *the coupled method* and the second *the decoupled method*. We solve the SKIEs using a Nyström method with GMRES, which requires evaluating layer potentials at the boundary using a suitable singular quadrature scheme. For our numerical experiments, we use quadrature-by-expansion (QBX) with fast-multipole acceleration [5, 18]. Consequently, both methods have linear complexity with respect to the number of degrees of freedoms. It is noteworthy that our methods are agnostic of the singular quadrature scheme. Our methods are also capable of using high order discretization and can handle complex geometries. We demonstrate this through numerical examples in two and three dimensions.

The rest of this paper is organized as follows. We first present the derivation for the free-space Green's functions and the decoupling transform in Section 2. Then we give the SKIE formulations for both the decoupled and coupled methods in Section 3, and present some details of our numerical implementation in Section 4. After that, we present the numerical results in Section 5, and give some concluding discussion in Section 6.

2. Analysis of the problem

2.1. Thermal and acoustic modes

In order to obtain an integral equation formulation, we require the free-space Green's function for the Morse-Ingard equations (1). Following the derivation for the analytic solution to the Morse-Ingard equations in a cylindrically symmetric geometry in [4], we first identify the eigenmodes by looking for particular solutions where T is an eigenfunction of ∇^2, s.t. $\nabla^2 T = -k^2 T$. Substituting into the first equation of (1) yields

$$P = \frac{\gamma}{\gamma - 1}[(1 + i\Omega k^2)T + iS]. \tag{5}$$

Consider the homogeneous case by letting $S = 0$, then $P = mT$ is also an eigenfunction of ∇^2, where the constant $m = \frac{\gamma}{\gamma-1}(1 + i\Omega k^2)$. Substituting (5) and $P = mT$ into (1) yields

$$(1 - i\gamma\Lambda)(-k^2 mT) + \left[\gamma\left(1 - \frac{\Lambda}{\Omega}\right) + \frac{\Lambda}{\Omega}\right](mT) - \gamma\left(1 - \frac{\Lambda}{\Omega}\right)T = 0. \tag{6}$$

For (6) to have nontrivial solution, the coefficient of T must vanish, so that

$$(i\Omega + \gamma\Omega\Lambda)k^4 + (1 - i\gamma\Omega - i\Lambda)k^2 - 1 = 0. \tag{7}$$

Let Q to be a complex constant such that $Q^2 = 4(i\Omega+\gamma\Omega\Lambda)+(1-i\gamma\Omega-i\Lambda)^2$. Based on physical interpretation, we classify the roots of (7) into two groups:

1. k_t corresponding to the thermal modes that attenuate rapidly:

$$k_t^2 = \frac{i}{2\Omega}\left(\frac{1 - i\gamma\Omega - i\Lambda + Q}{1 - i\gamma\Lambda}\right), \quad m_t := \frac{\gamma}{\gamma - 1}(1 + i\Omega k_t^2). \tag{8}$$

2. k_p corresponding to the acoustic modes that attenuate slowly:

$$k_p^2 = \frac{i}{2\Omega}\left(\frac{1 - i\gamma\Omega - i\Lambda - Q}{1 - i\gamma\Lambda}\right), \quad m_p := \frac{\gamma}{\gamma - 1}(1 + i\Omega k_p^2). \tag{9}$$

Since the eigenfunctions of ∇^2 form a basis of H^1, we obtain the fundamental set of solutions to the homogeneous problem under radial symmetry, denoted U_d, $(d = 2, 3)$,

$$\begin{bmatrix} T(r) \\ P(r) \end{bmatrix} \in U_d.$$

In two dimensions ($d = 2$),

$$U_2 = \operatorname{span}\left\{ \begin{bmatrix} J_0(k_p r) \\ m_p J_0(k_p r) \end{bmatrix}, \begin{bmatrix} H_0^{(1)}(k_p r) \\ m_p H_0^{(1)}(k_p r) \end{bmatrix}, \begin{bmatrix} J_0(k_t r) \\ m_t J_0(k_t r) \end{bmatrix}, \begin{bmatrix} H_0^{(1)}(k_t r) \\ m_t H_0^{(1)}(k_t r) \end{bmatrix} \right\}, \tag{10}$$

where J_0 is the Bessel function of the first kind of order zero, $H_0^{(1)}$ is the Hankel function of the kind of order zero. Similarly, in three dimensions ($d = 3$),

$$U_3 = \operatorname{span}\left\{ \begin{bmatrix} j_0(k_p r) \\ m_p j_0(k_p r) \end{bmatrix}, \begin{bmatrix} h_0^{(1)}(k_p r) \\ m_p h_0^{(1)}(k_p r) \end{bmatrix}, \begin{bmatrix} j_0(k_t r) \\ m_t j_0(k_t r) \end{bmatrix}, \begin{bmatrix} h_0^{(1)}(k_t r) \\ m_t h_0^{(1)}(k_t r) \end{bmatrix} \right\}, \tag{11}$$

where j_0 is the spherical Bessel function of the first kind of order zero, $h_0^{(1)}$ is the spherical Bessel function of the third kind of order zero. We also note that $h_0^{(1)}$ has simple closed form

$$h_0^{(1)}(r) = j_0(r) + i y_0(r) = \frac{\sin r}{r} - i\frac{\cos r}{r} = \frac{-i}{r} e^{ir}. \tag{12}$$

Note that the choice of basis is not unique. We deliberately chose the above basis functions so that the condition in (3) can be easily enforced.

2.2. The decoupled equations

From the above radial symmetry solutions, it is obvious that the Morse-Ingard equations are a linear superposition of two Helmholtz-type equations. To get the actual change of variables that decouples the PDE system, we solve for $t \in \mathbb{C}$ such that the sum of the first equation and t times the second equation in (1) reduces to a scalar Helmholtz-type PDE

$$a_1(t)\nabla^2 T + a_2(t)\nabla^2 P + a_3(t) T + a_4(t) P = a_5(t) S, \tag{13}$$

where $a_1 = \Omega$, $a_2 = (1 - i\gamma\Lambda)t$, $a_3 = i - \gamma\left(1 - \frac{\Lambda}{\Omega}\right)t$, $a_4 = -i\frac{\gamma-1}{\gamma} + \left[\gamma\left(1 - \frac{\Lambda}{\Omega}\right) + \frac{\Lambda}{\Omega}\right]t$, $a_5 = 1 - i\gamma\frac{\Lambda}{\Omega}t$ are all linear functions of t. The condition under which (13) becomes a scalar Helmholtz-type PDE is $a_1 a_4 = a_2 a_3$, which is a quadratic equation of t and admits two roots

$$t_\pm = \frac{(2\Lambda\gamma - \Lambda - \Omega\gamma + i)\Omega \mp i\Omega Q}{2\gamma(\Lambda - \Omega)(i\Lambda\gamma - 1)}. \tag{14}$$

Letting $V_t = \Omega T + t_+(1 - i\gamma\Lambda)P$, $V_p = \Omega T + t_-(1 - i\gamma\Lambda)P$, we find the decoupled scalar PDEs,

$$\begin{aligned} \nabla^2 V_t + k_t^2 V_t &= a_5(t_+) S, \\ \nabla^2 V_p + k_p^2 V_p &= a_5(t_-) S, \end{aligned} \tag{15}$$

as expected from the thermal and acoustic modes.

2.3. Sommerfeld radiation condition

Now we consider the boundary conditions for the decoupled equations (15). The boundary conditions on ∂D are still decoupled Neumann,

$$\begin{aligned} \left.\frac{\partial V_t}{\partial n}\right|_{\partial D} &= \Omega g_T + t_+(1-i\gamma\Lambda)g_P, \\ \left.\frac{\partial V_p}{\partial n}\right|_{\partial D} &= \Omega g_T + t_-(1-i\gamma\Lambda)g_P. \end{aligned} \tag{16}$$

For the far-field conditions, we can either impose boundedness of V_t, V_p at infinity, or apply the classical far-field conditions for the Helmholtz equation due to Arnold Sommerfeld,

$$\begin{aligned} \lim_{|x|\to\infty} |x|^{\frac{d-1}{2}} \left(\frac{\partial}{\partial |x|} - ik_t\right) V_t &= 0, \\ \lim_{|x|\to\infty} |x|^{\frac{d-1}{2}} \left(\frac{\partial}{\partial |x|} - ik_p\right) V_p &= 0. \end{aligned} \tag{17}$$

2.4. Free-space Green's function

By letting $S = \delta(r)$ in (1), the free-space Green's function satisfies the following equations in the weak sense,

$$\begin{cases} \Omega\nabla^2 T + iT - i\dfrac{\gamma-1}{\gamma}P = \delta, \\ (1-i\gamma\Lambda)\nabla^2 P + \left[\gamma\left(1-\dfrac{\Lambda}{\Omega}\right) + \dfrac{\Lambda}{\Omega}\right]P - \gamma\left(1-\dfrac{\Lambda}{\Omega}\right)T = -i\gamma\dfrac{\Lambda}{\Omega}\delta. \end{cases} \tag{18}$$

We first seek for weak solutions $[T(r), P(r)]^T \in U_d$ that also satisfy the far-field conditions in (3). In two dimensions, because when k has positive imaginary part, solutions with nonzero J_0 components are unbounded at infinity, and represent a wave traveling from infinity towards 0, enforcing the far-field conditions amounts to restricting the solution to the two-dimensional subspace of U_2 spanned by bases involving $H_0^{(1)}$. Similarly, we restrict the solution to the two-dimensional subspace of U_3 spanned by bases involving $h_0^{(1)}$ in 3D.

We note that, in the weak sense, $\nabla^2_{2D}\left(\frac{1}{2\pi}\ln r\right) = \nabla^2_{3D}\left(-\frac{1}{4\pi}\frac{1}{r}\right) = \delta(r)$. The following asymptotic limits hold when $r \to 0$ ([13]),

$$\nabla^2_{2D} H_0^{(1)}(kr) \sim \nabla^2[(2i/\pi)\ln(kr)] = 4i\delta(r), \tag{19}$$

$$\nabla^2_{3D} h_0^{(1)}(kr) \sim \nabla^2[-i/(kr)] = (4\pi i/k)\delta(r). \tag{20}$$

When $r \neq 0$, any linear combination in the fundamental set U_d solves the system. All we need is to match the leading order terms in the neighborhood of 0. Since we have restricted the solutions to a two-dimensional space, matching the two coefficients on the right hand side of (18) uniquely determines the Green's function.

2.4.1. 2D

In two dimensions, we let

$$\begin{aligned} G_T &= b_1 H_0^{(1)}(k_p r) + b_2 H_0^{(1)}(k_t r), \\ G_P &= b_1 m_p H_0^{(1)}(k_p r) + b_2 m_t H_0^{(1)}(k_t r). \end{aligned} \tag{21}$$

Substituting into (18) and matching the leading order terms yields

$$\begin{aligned} &4i\Omega(b_1 + b_2)\delta = \delta, \\ &4i(1 - i\gamma\Lambda)(b_1 m_p + b_2 m_t)\delta = -i\gamma\frac{\Lambda}{\Omega}\delta. \end{aligned} \tag{22}$$

Solving this linear system, we have

$$\begin{aligned} b_1 &= \frac{\gamma - 1}{4\gamma\Omega Q}[i m_t + (m_t - 1)\gamma\Lambda], \\ b_2 &= -\frac{\gamma - 1}{4\gamma\Omega Q}[i m_p + (m_p - 1)\gamma\Lambda]. \end{aligned} \tag{23}$$

2.4.2. 3D

Similarly, in three dimensions, we let

$$\begin{aligned} G_T &= c_1 h_0^{(1)}(k_p r) + c_2 h_0^{(1)}(k_t r), \\ G_P &= c_1 m_p h_0^{(1)}(k_p r) + c_2 m_t h_0^{(1)}(k_t r). \end{aligned} \tag{24}$$

Substituting into (18) and matching the leading order terms yields

$$\begin{aligned} &4\pi i\Omega\left(\frac{c_1}{k_p} + \frac{c_2}{k_t}\right)\delta = \delta \\ &4\pi i(1 - i\gamma\Lambda)\left(\frac{c_1 m_p}{k_p} + \frac{c_2 m_t}{k_t}\right)\delta = -i\gamma\frac{\Lambda}{\Omega}\delta. \end{aligned} \tag{25}$$

The solution is

$$\begin{aligned} c_1 &= \frac{k_p(\gamma - 1)}{4\pi\gamma\Omega Q}[i m_t + (m_t - 1)\gamma\Lambda], \\ c_2 &= -\frac{k_t(\gamma - 1)}{4\pi\gamma\Omega Q}[i m_p + (m_p - 1)\gamma\Lambda]. \end{aligned} \tag{26}$$

2.5. Green's representation formula

Since the solution to the Helmholtz equation satisfies Green's representation formula, we expect a similar relation holds for solution to the Morse-Ingard equations as well. Let G_p, G_t be the Helmholtz kernels of wave number k_p, k_t, respectively. Given a density $\rho \in C(\partial D)$, define the *single-layer potential operators*

$$\begin{aligned} S_t[\rho](x) &= \int_{\partial D} G_t(x,y)\rho(y) ds_y, \\ S_p[\rho](x) &= \int_{\partial D} G_p(x,y)\rho(y) ds_y, \end{aligned} \tag{27}$$

and the *double-layer potential operators*

$$\begin{aligned} D_t[\rho](x) &= \int_{\partial D} \partial_{n_y} G_t(x,y)\rho(y) ds_y, \\ D_p[\rho](x) &= \int_{\partial D} \partial_{n_y} G_p(x,y)\rho(y) ds_y. \end{aligned} \tag{28}$$

If $x \in \partial D$, the integrals above are to be understood in the principal-value sense.

Let D be a bounded region in $\mathbb{R}^n$, and ∂D is piecewise C^2. Then from Green's representation formula for the Helmholtz equation [3, Theorem 12], for all $x \in D$,

$$\begin{aligned} D_t[V_t] - S_t[\partial_n V_t] &= -V_t, \\ D_p[V_p] - S_p[\partial_n V_p] &= -V_p. \end{aligned} \tag{29}$$

Denote the left hand sides of (29) as $L_t[V_t]$ and $L_p[V_p]$, respectively. Recalling that $V_{t,p} = \Omega T + t_\pm(1 - i\gamma\Lambda)P$, we have

$$\begin{aligned} \Omega L_t[T] + t_+(1 - i\gamma\Lambda) L_t[P] &= -\Omega T - t_+(1 - \gamma\Lambda)P, \\ \Omega L_p[T] + t_-(1 - i\gamma\Lambda) L_p[P] &= -\Omega T - t_-(1 - \gamma\Lambda)P, \end{aligned} \tag{30}$$

inside D. (30) gives representations of P and T in terms of layer potentials. Lastly, we note that since all layer potentials above are zero at infinity, the assumption that D is bounded can be removed and (30) still holds.

3. SKIE formulations

3.1. The decoupled method

As demonstrated above, the Morse-Ingard equations can be decoupled into two Helmholtz-like PDEs that have decoupled Neumann boundary conditions on ∂D. The most straightforward scheme is to solve the decoupled

PDEs separately and recombine the results. Both decoupled equations have the form

$$\begin{cases} \nabla^2 V + k^2 V = 0, & \text{in } D^c, \\ \partial_n V = h, & \text{on } \partial D, \end{cases} \tag{31}$$

where $V \in \{V_t, V_p\}$, $k \in \{k_t, k_p\}$, $h = \Omega g_T + t_\pm(1 - i\gamma\Lambda)g_P$, respectively.

We solve (31) using a single-layer potential representation. For $x \in \partial D$, let

$$\begin{aligned} V_t(x) = S_t[\sigma_t](x) = \mathrm{PV}\int_{\partial D} \overline{G}(k_t|x-y|)\sigma_t(y)ds_y, \\ V_p(x) = S_p[\sigma_p](x) = \mathrm{PV}\int_{\partial D} \overline{G}(k_p|x-y|)\sigma_p(y)ds_y, \end{aligned} \tag{32}$$

where $\sigma_{t,p} \in L^2(\partial D)$, $\overline{G}(r) = \frac{1}{2\pi}\ln r$ in $2D$ and $\overline{G}(r) = -\frac{1}{4\pi r}$ in $3D$. This leads to the following SKIE for each decoupled component [1],

$$-\frac{1}{2}\sigma(x) + \mathrm{PV}\int_{\partial D} \partial_n \overline{G}(k|x-y|)\sigma(y)ds_y = h(x), \quad \text{on } \partial D. \tag{33}$$

After obtaining V_t, V_p, we then recover T, P by applying the inverse change of variables

$$\begin{bmatrix} T \\ P \end{bmatrix} = \begin{bmatrix} \Omega & t_+(1-i\gamma\Lambda) \\ \Omega & t_-(1-i\gamma\Lambda) \end{bmatrix}^{-1} \begin{bmatrix} V_t \\ V_p \end{bmatrix}. \tag{34}$$

3.2. The coupled method

Alternatively, we can also use the Green's function for the Morse-Ingard equations to directly formulate a coupled SKIE. Denote the free-space Green's functions in 2/3D by

$$G(r) = \begin{bmatrix} G_T(r) \\ G_P(r) \end{bmatrix}. \tag{35}$$

We assume that $k_t^2 - k_p^2 = -\frac{Q}{\Omega(i+\gamma\Lambda)} \neq 0$, which is well-justified on physical grounds (the thermal and acoustic waves have fundamentally different properties). Then,

$$G_1(r) = -\frac{\alpha_1 \Omega(1-i\gamma\Lambda)}{4b_2 Q}(\nabla^2 + k_p^2)G(r), \tag{36}$$

where $\alpha_1 = 1$ in 2D, and $\alpha_1 = \frac{k_t}{\pi}$ in 3D. And let

$$G_2(r) = \frac{\alpha_2 \Omega(1-i\gamma\Lambda)}{4b_1 Q}(\nabla^2 + k_t^2)G(r), \tag{37}$$

where $\alpha_2 = 1$ in 2D, and $\alpha_2 = \frac{k_p}{\pi}$ in 3D.

Obviously, G_1, G_2 satisfy the homogeneous PDE when $r \neq 0$ because they consist of G and its derivatives. In fact, they are constructed to have very simple explicit formulae:

$$G_1(r) = -\frac{1}{4i}\begin{bmatrix} H_0^{(1)}(k_t r) \\ m_t H_0^{(1)}(k_t r) \end{bmatrix}, \quad G_2(r) = -\frac{1}{4i}\begin{bmatrix} H_0^{(1)}(k_p r) \\ m_p H_0^{(1)}(k_p r) \end{bmatrix} \quad \text{in 2D}, \tag{38}$$

and

$$G_1(r) = -\frac{k_t}{4\pi i}\begin{bmatrix} h_0^{(1)}(k_t r) \\ m_t h_0^{(1)}(k_t r) \end{bmatrix}, \quad G_2(r) = -\frac{k_p}{4\pi i}\begin{bmatrix} h_0^{(1)}(k_p r) \\ m_p h_0^{(1)}(k_p r) \end{bmatrix} \quad \text{in 3D}. \tag{39}$$

To account for the two boundary conditions in (2), we need two scalar densities. Let $\sigma = [\sigma_1, \sigma_2]^T$, $\sigma_i \in L^2(\partial D)$. Define the (vector-valued) single-layer potentials of a scalar density ρ to be

$$S_i[\rho](x) = \mathrm{PV}\int_{\partial D} G_i(|x-y|)\rho(y)ds_y, \quad x \in \partial D, \text{ and } i = 1, 2. \tag{40}$$

We consider the following solution representation

$$u = S_1[\sigma_1] + S_2[\sigma_2]. \tag{41}$$

We claim that (41) gives an SKIE for the Morse-Ingard equation. To show that, we first present the jump relations of the layer potential operators used in the construction.

Proposition 1 (Jump relations)**.** *$S_i[\sigma_i]$ is continuous across ∂D, and its normal derivative satisfies the following jump relations: for $z \in \partial D$,*

$$\frac{\partial}{\partial n_z}S_i(z)_\pm := \lim_{x\to z\pm}\frac{\partial}{\partial n_z}S_i[\sigma_i](x) = \frac{\partial}{\partial n_z}S_i[\sigma_i](z) \mp \frac{1}{2}\begin{bmatrix} c_i \\ d_i \end{bmatrix}\sigma_i(z), \tag{42}$$

where

$$\begin{aligned} &c_1 = c_2 = 1, \quad d_1 = m_t, \quad d_2 = m_p \quad \textit{in } 2D, \\ &c_1 = \frac{1}{k_t}, \quad c_2 = \frac{1}{k_p} \quad , d_1 = \frac{m_t}{k_t}, \quad d_2 = \frac{m_p}{k_p} \quad \textit{in } 3D. \end{aligned} \tag{43}$$

Since in our construction, the layer potential operators are standard single-layer potentials of the Helmholtz equation (up to constant multiplications), the proof of (1) follows the same exact steps as in [1, Chapter 2.4-2.5] for the Helmholtz equation.

Substituting the representation of u into (2) yields the following boundary integral equation

$$\left(-\frac{1}{2}\begin{bmatrix} c_1 & c_2 \\ d_1 & d_2 \end{bmatrix} + \begin{bmatrix} \partial_n S_{1T} & \partial_n S_{2T} \\ \partial_n S_{1P} & \partial_n S_{2P} \end{bmatrix}\right)\begin{bmatrix} \sigma_1 \\ \sigma_2 \end{bmatrix}(z) = \begin{bmatrix} \partial_n T \\ \partial_n P \end{bmatrix}(z), \quad \forall z \in \partial D. \tag{44}$$

Note that under the current assumption of $k_t^2 \neq k_p^2$, we have

$$\det\left(\begin{bmatrix} c_1 & c_2 \\ d_1 & d_2 \end{bmatrix}\right) = c_1 d_2 - c_2 d_1 \neq 0. \tag{45}$$

To supply smoothness for our proofs of numerical accuracy, we note a compactness result for the operators in (44).

Proposition 2. *If $\partial D \in C^2$, for $0 < \alpha < 1$, the operator*

$$L : \begin{bmatrix} \sigma_1 \\ \sigma_2 \end{bmatrix} \mapsto \begin{bmatrix} \partial_n S_{1T} & \partial_n S_{2T} \\ \partial_n S_{1P} & \partial_n S_{2P} \end{bmatrix}\begin{bmatrix} \sigma_1 \\ \sigma_2 \end{bmatrix}$$

is a compact operator from $C^{0,\alpha} \times C^{0,\alpha}$ into itself.

Proof. Since L is a 2×2 operator matrix, we only need to show that each entry is compact. Being adjoint operators of the double layer potentials (i.e., derivatives of rescaled Helmholtz single layer potentials), $\partial_n S_{i*}$ are compact operators from Hölder space $C^{0,\alpha}(\partial D)$ into itself ([9, Theorem 7.5]). Therefore, (44) is an SKIE. ☐

Regarding analytical properties of the operator, the most relevant results we found in the literature are for layer potentials with Laplace kernels, which admit the following regularity estimates:

Proposition 3 (Layer potential regularity [10, Prop. 4.2])**.** *Let $d \geq 2$, $p \in (1, \infty)$, and $p(\ell - 1) > d - 1$, where ℓ is a noninteger, $\ell > 1$. And let $\alpha = 1 - \{\ell\} - 1/p$. Suppose that ∂D is connected and satisfies the Sobolev graph property $\partial D \in W_p^\ell$, that is, for every point $O \in \partial D$ there exists a neighbourhood U and $f \in W_p^\ell(\mathbb{R}^{d-1})$ such that*

$$U \cap \Omega = U \cap \{(x, y) | x \in \mathbb{R}^{d-1}, y > f(x)\}.$$

Then

$$\|(S\rho)_+\|_{W_p^{\lfloor \ell \rfloor + 1, \alpha}(D)} \leq c\|\rho\|_{W_p^{\ell - 1}(\partial D)},$$
$$\|(S\rho)_-\|_{W_p^{\lfloor \ell \rfloor + 1, \alpha}(D)} \leq c(D)\|\rho\|_{W_p^{\ell - 1}(\partial D)},$$

where the weighted Sobolev norm is defined as

$$\|u\|_{W_p^{m,\alpha}(D)} = \left(\int_D (\mathrm{dist}(z, \partial D))^{p\alpha} |\nabla_m u(z)|^p dz\right)^{1/p} + \|u\|_{L_p(D)},$$

and $(S\rho)_\pm$ *are the limits of the Laplace single layer potentials from the outside and the inside, respectively. In particular, for the adjoint operator,*

$$\|D^\star \rho\|_{W_p^{\ell-1}(\partial D)} \leq c\|\rho\|_{W_p^{\ell-1}(\partial D)}.$$

4. Numerical implementation and error analysis

For the coupled method, the left hand side operator of the SKIE is a compact perturbation to a block-constant operator. This structure inspires us to try to use the inverse of the constant part in (44) as a left block preconditioner

$$P = \left(-\frac{1}{2}\begin{bmatrix} c_1 & c_2 \\ d_1 & d_2 \end{bmatrix}\right)^{-1}. \tag{46}$$

The idea is to make the preconditioned operator "almost" block-diagonal in the sense that its spectrum only has one cluster point in the complex plane, as will be shown in the numerical tests. Doing so empirically reduces the number of GMRES iterations needed by up-to one half.

As will be shown in the next section, for the realistic parameters used in our tests, the thermal modes decay rapidly relative to the acoustic modes, leading to two widely separated spatial scales. This may lead to numerical difficulties for the coupled method. Due to the fast decay of thermal modes, however, if we are only interested in the solution in the bulk region away from the boundary, we can solve only for V_p in (31) using a single-layer potential representation

$$V_p(x) = S_p[\sigma_p](x) = \mathrm{PV}\int_{\partial D} \overline{G}(k_p|x-y|)\sigma_p(y)ds_y, \quad x \in \partial D, \tag{47}$$

and then obtain T and P by fixing thermal mode to be zero and applying the inverse change of variables

$$\begin{bmatrix} T \\ P \end{bmatrix} = \begin{bmatrix} \Omega & t_+(1-i\gamma\Lambda) \\ \Omega & t_-(1-i\gamma\Lambda) \end{bmatrix}^{-1} \begin{bmatrix} 0 \\ V_p \end{bmatrix}. \tag{48}$$

Since doing so equates to projecting the problem to include only the acoustic modes, we will refer to this modified version of the decoupled method as *the projection method.*

The recasting of the Morse-Ingard system (1) in second-kind integral equations presented thus far is independent of the specific means by which it is discretized.

We discretize the SKIEs using the Nyström's approach, that is, we discretize (44) by replacing the (singular) integrals in the layer potential operators by appropriate quadrature schemes. To evaluate the singular quadratures efficiently, we use the GIGAQBX algorithm, a quadrature-by-expansion method with FMM acceleration [5, 15, 18]. With efficient algorithms for the left hand side operators, we solve the discretized linear systems using GMRES.

Loosely, for Nyström discretizations of second-kind systems, Anselone's theorem (e.g. [9, Theorem 10.12]) states that the error in the computed density is bounded by the sum of the discretization error in the right-hand side and the quadrature error in the evaluation of the layer potential operators. Given our use of QBX discretization, our quadrature error behaves as described by the following theorem:

Theorem 4 (QBX error estimate [5, Thm. 1])**.** *Suppose that* ∂D *is a smooth, bounded curve embedded in* $\mathbb{R}^2$*, that* $B_r(c)$ *is the ball of radius* r *about* c*, and that* $\overline{B_r(c)} \cap \partial D = \{x\}$*. Let* ∂D *be divided into* M *panels, each of length* h *and let* p, q *be non-negative integers that define the QBX order and the number of nodes of the smooth Gaussian quadrature used to compute the QBX coefficients, respectively. For* $0 < \beta < 1$*, there are constants* $C_{p,\beta}$ *and* $\tilde{C}_{p,q,\beta}$ *so that if* ϕ *lies in the Hölder space* $C^{p,\beta}(\partial D) \cap C^{q,\beta}(\partial D)$*, then the components of QBX discretization error admit the following bounds*

$$\|E_{QBX,trunc}(\phi)\|_\infty \le C_{\partial D,p,\beta} r^{p+1} \|\phi\|_{C^{p,\beta}(\partial D)}, \tag{49}$$

$$\|E_{QBX,quad}(\phi)\|_\infty \le \tilde{C}_{\partial D,p,q,\beta} \left(\frac{h}{4r}\right)^q \|\phi\|_{C^{q,\beta}(\partial D)}. \tag{50}$$

The use of layer potentials (such as $\partial_n S$) with more derivatives as well as the use of FMM approximation incurs additional (controlled) error. See, for example, [2] as well as the FMM error analysis in [19] for details.

5. Numerical results

In this section, we present several numerical examples that demonstrate the accuracy and efficiency of our method. The dimensionless parameter values used for all our tests are listed in Table 1, which are derived from the physical parameters from [4]. This set of parameters assumes that the fluid is nitrogen gas at a temperature of 300 K and a pressure of 1 bar. It is noteworthy that the parameter values we use closely correspond to the modeling of laboratory experiments of trace gas sensors [14].

Symbol	Value
Ω	$3.664152973215096 \times 10^{-5}$
γ	1.399999976158142
Λ	$5.370572762330994 \times 10^{-5}$

Table 1: Dimensionless parameters.

Using these dimensionless parameters to solve (6) yields the two wavenumbers

$$k_t \approx 116.81 + 116.81i,$$
$$k_p \approx 1 + 3.42 \times 10^{-5} i.$$

We note that k_t is the wavenumber corresponding to the fast-decaying thermal modes, which gives rise to a boundary layer with thickness at the scale of $\frac{1}{|\mathrm{Im}\, k_t|} \approx 0.01$. On the other hand, k_p corresponds to the slowly-decaying acoustic modes that have characteristic length at the scale of 1.

In all our tests, the GMRES tolerance is set to 10^{-14}. We denote the computed temperature field T_h and the pressure field P_h, respectively, and let

$$E_T(x) = \frac{|T_h(x) - T(x)|}{|T(x)|}, \quad E_P(x) = \frac{|P_h(x) - P(x)|}{|P(x)|}. \tag{51}$$

5.1. The coupled method and preconditioning

We perform convergence tests on a two-dimensional circular geometry with radius 3.5 centered at $(5.25, 5.25)$. The manufactured solution is obtained by evaluating a point potential using the free-space Green's function in Section 2.4 from sources inside the circle. We use piecewise polynomials up to order p to discretize over each panel. For each test, we measure the error in the infinity norm on the boundary discretization points as well as some volume points in $[0, 10.5]^2 \setminus D$.

We first perform p-convergence tests by splitting the circle into 100 equal-sized panels and increase p. For this test, we set the values for the FMM order and the QBX order to also be p for simplicity. Note that both the FMM order and the QBX order are linear functions of the number of accurate digits, and setting them to be equal is by no means the optimal choice, but does not affect the asymptotic convergence behavior. Results for the coupled method are shown in Figure 1. In the first place, we see similar convergence curves for different ways to measure the error norm, while the error data measured over the boundary is less noisy. Therefore, from now on, we will only measure the error over the boundary. We also see similar convergence curves when we solve with or without the block preconditioner.

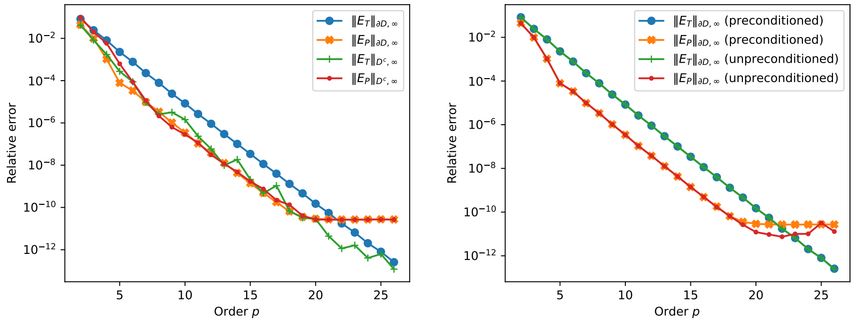

Figure 1: p-convergence using the coupled method. (Left: comparing the error norms measured over the boundary versus the volume. Right: comparing the errors with and without using the block preconditioner.)

We also perform h-convergence tests by fixing p and shrinking panel sizes. For this test, we set the QBX order to be $p+4$ and fix FMM order to be 15. The goal for such choices is to make the QBX truncation error and FMM error much smaller than the discretization error; therefore, we should have convergence order of $p+1$ as $h \to 0$. The results are shown in Figure 2, where the data confirms our expected convergence order.

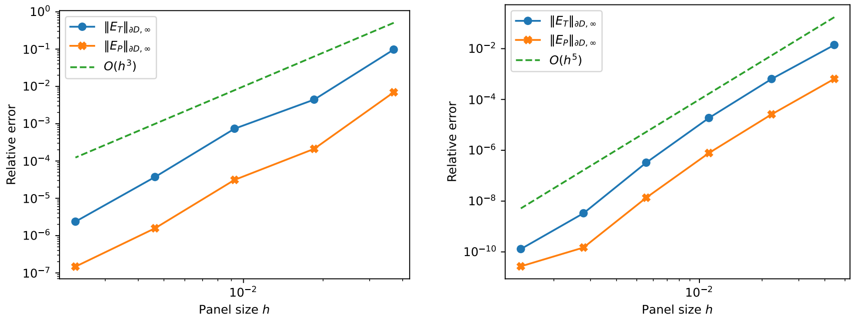

Figure 2: h-convergence using the coupled method. (Left: $p = 2$. Right: $p = 4$.)

5.2. *The coupled method vs the decoupled method*

Using the same problem setup as in Section 5.1, we compare the coupled method and the decoupled method. We present the results in Figure 3. For low order cases, the decoupled method yields accuracy comparable to the coupled method; however, as we increase resolution, the coupled method can achieve 10^{-12} accuracy, while convergence for the decoupled method stalls at around 10^{-7}. This phenomenon can be explained by the large condition number of the decoupling transform,

$$\kappa\left(\begin{bmatrix}\Omega & t_+(1-i\gamma\Lambda)\\ \Omega & t_-(1-i\gamma\Lambda)\end{bmatrix}\right)\approx 4.19\times 10^4.$$

For all three methods, the number of iterations needed does not increase as we increase the resolution, which is as expected due to our formulations being second-kind. Furthermore, the block preconditioner reduces the iteration count significantly with little added cost. Roughly speaking, the decoupled method requires similar number of GMRES iterations as the preconditioned coupled method.

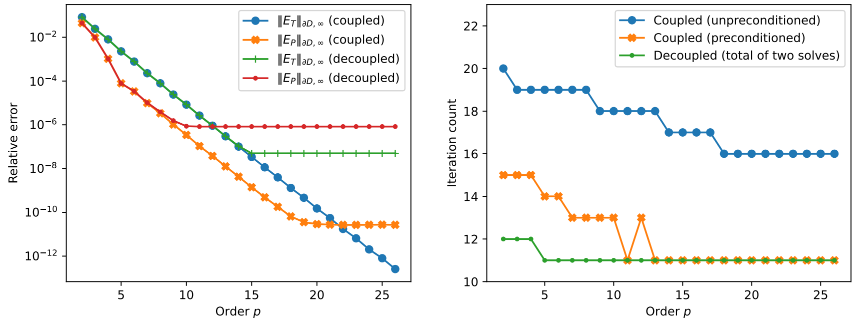

Figure 3: The coupled vs the decoupled method. (Left: convergence when increasing order. Right: total number of GMRES iterations.)

To further illustrate the effects of the left block preconditioner, we plot the spectrum of the linear system with and without it in Figure 4, all other parameters fixed. As expected, we see that the preconditioner causes the spectrum to cluster at one location in the complex plane instead of two. This effect explains the reduction factor of iteration counts.

5.3. *The projection method for solution in the bulk region*

The projection method (48) is a variant of the decoupled method for solution away from the boundary. To test how it performs, we use it to find

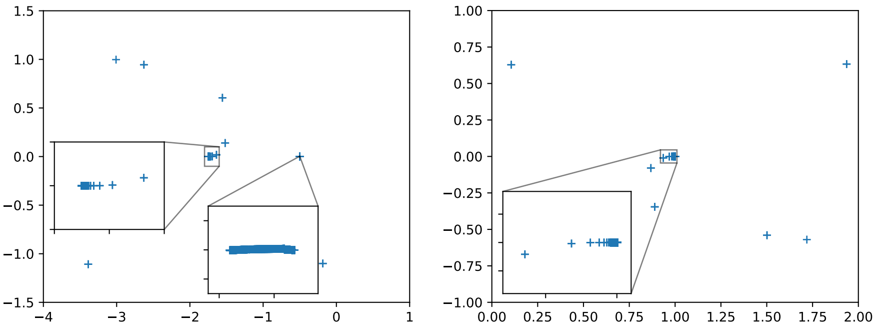

Figure 4: Spectra of the coupled method over the complex plane, where the abscissa and the ordinate correspond to the real and imaginary parts, respectively. Enlarged views of regions surrounding the cluster points are highlighted within rectangular boxes. (Left: without left block preconditioning. Right: with left block preconditioning.)

the solution over $[0, 10.5]^2 \setminus D$, where D is as shown in the left plot of Figure 5. The red dots marks the point sources used to produce the manufactured solution. The lower-left half shows the relative error of the temperature field E_T, while the upper-right half shows the relative error of the pressure field E_P. As expected, the solution away from the boundary is accurate.

To see how the error decays with respect to the distance from boundary, in the right plot of Figure 5, we plot the l_∞ norms of the relative errors over a set of equidistant curves against the curves' distance from ∂D. We observe that the errors decay exponentially with respect to the distance from boundary. For this example, the projected solution is indistinguishable from the non-projected solution where the distance is greater than 0.1, which is only 1.6% of the acoustic wave length. Therefore, if the goal is to obtain solution in the bulk region, the projection method can be very advantageous because it does not need to resolve the length scale of the thermal boundary layer.

It is worth pointing out that because V_p is a linear combination of temperature and pressure, by projecting the solution into only acoustic modes, we are still solving a model with thermoacoustic coupling.

5.4. Torus with the coupled method

We apply the preconditioned coupled method to solve on a torus geometry with major radius 0.7 and minor radius 0.07 as shown in Figure 6. For the discretization, we set the mesh size $h = 0.02$, discretization order $p = 4$, QBX order 10, and FMM order 15. Note that when computing layer potentials, it is unusual to set the QBX order to be much higher than the

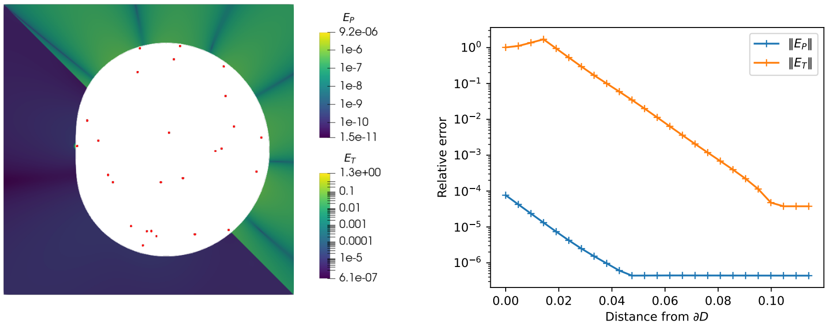

Figure 5: Error using the projection method. (Left: showing the geometry and relative error E_T (lower-left), E_P (upper-right). Right: showing that error decays exponentially w.r.t. the distance from the boundary.)

discretization order like this. The reason for the excessive QBX order here is to resolve the boundary layer. The discrete system has roughly 1.97 million unknowns. The errors over the boundary are $\|E_T\|_{\partial D} = 3.20 \times 10^{-3}$, $\|E_P\|_{\partial D} = 1.74 \times 10^{-3}$. In Figure 6, part of the torus surface is shown in a "cut-off" manner to reveal the source point that gives rise to the manufactured solution. The rest of the torus surface shows a color map of the residual. And the plane surfaces behind the torus show a color map of $\max(E_T, E_P)$ in the volume.

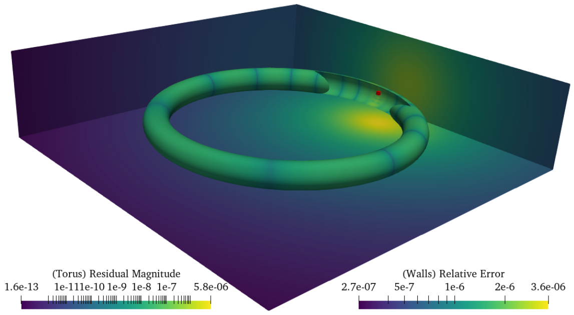

Figure 6: Torus with the coupled method.

5.5. A tuning fork geometry with the projection method

When only the solution away from the boundary is needed, the projection method allows solving for large problems that are otherwise too expensive to be solved with the coupled method by circumventing the need to resolve the boundary layer. In this test, we solve over a tuning fork geometry as shown in Figure 7 using the projection method. The size of the tuning fork is roughly $1.5 \times 0.34 \times 6.23$. Since there is no boundary layer in the acoustic modes, we use a QBX order of 2 and FMM order 15. The discrete system has roughly 2.7 million unknowns. In Figure 7, part of the tuning fork surface is made transparent to reveal the source points that give rise to the manufactured solution. The remaining part of the tuning fork is colored by the residual magnitude. Also, the plane surfaces behind the tuning fork show a color map of $\max(E_T, E_P)$ in the volume. Although the error is large on the boundary surface ($\|E_T\|_{\partial D} = 1.00$, $\|E_P\|_{\partial D} = 0.01$), the solution in the bulk region has five digits of accuracy, as shown in Figure 8.

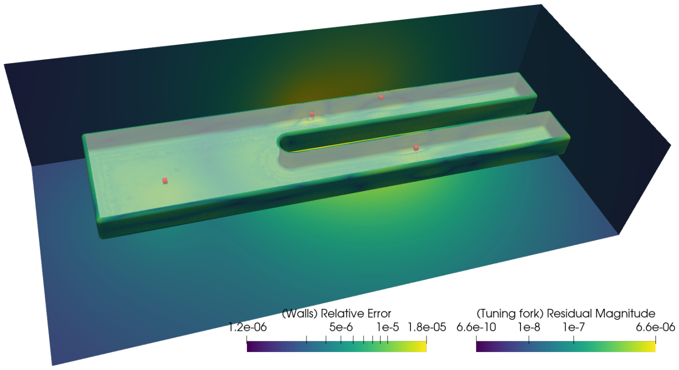

Figure 7: Tuning fork with the projection method.

6. Conclusion

In this work, we have derived the free-space Green's function and the decoupled PDE form of the Morse-Ingard equations. Our results are an extension of the analysis in [4]. Using the obtained relation between the Morse-Ingard equations and the Helmholtz equations, we have provided analogs of the Sommerfeld radiation conditions and Green's representation formulae for the Morse-Ingard equations. Based on our analysis, we have developed three integral equations methods for the Neumann problem of the Morse-Ingard

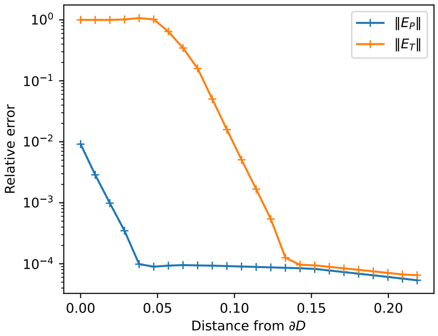

Figure 8: Error of the tuning fork solution decays with increasing distance from the boundary.

equations in the exterior domain: the (preconditioned) coupled method, the decoupled method, and the projection method. All three methods are based on SKIE formulations, and can be solved with linear complexity in the number of discretization nodes, as demonstrated in our numerical experiments using the GIGAQBX algorithm.

Through numerical tests using realistic parameter values, we have shown that for all three methods, the number of GMRES iterations does not grow with the problem size. Of the three methods, the coupled method is the best-conditioned and can achieve more than 11 digits of accuracy with sufficient resolution. In comparison, the decoupled method requires less computational cost, but it is prone to the ill-conditioning of the decoupling transform, which depends on the equation parameters. The projection method represents a trick applied to the decoupled method that can be used to circumvent the need to resolve the boundary layer when only the solution away from the boundary is desired. This is similar to the workaround used in [20] for long-time simulations.

It has been repeatedly observed that layer potentials with boundary layers are resolution-hungry and pose challenges in developing more efficient integral-equation-based solvers for such problems. For future research, we will look to improve the QBX method to more efficiently resolve boundary layers.

7. Acknowledgments

We would like to thank Professor John Zweck and Doctor Artur Safin for useful discussions on the model and boundary conditions. Our thanks also goes to Jacob Davis for sharing preliminary derivations related to the Greens function.

The first two authors' research was supported by the National Science Foundation under award numbers SHF-1911019 and OAC-1931577 as well as by the Department of Computer Science at the University of Illinois at Urbana-Champaign. The third author was supported by the National Science Foundation under award numbers SHF-1909176.

References

[1] David Colton and Rainer Kress. *Integral Equation Methods in Scattering Theory*. Classics in Applied Mathematics. Society for Industrial and Applied Mathematics, November 2013.

[2] Charles L. Epstein, Leslie Greengard, and Andreas Klöckner. On the Convergence of Local Expansions of Layer Potentials. *SIAM J. Numer. Anal.*, 51(5):2660–2679, January 2013.

[3] Lawrence Evans. *Partial Differential Equations, Second Edition*, volume 19 of *Graduate Studies in Mathematics*. American Mathematical Society, March 2010.

[4] Jordan Kaderli, John Zweck, Artur Safin, and Susan E. Minkoff. An analytic solution to the coupled pressure–temperature equations for modeling of photoacoustic trace gas sensors. *Journal of Engineering Mathematics*, 103(1):173–193, April 2017.

[5] Andreas Klöckner, Alexander Barnett, Leslie Greengard, and Michael O'Neil. Quadrature by expansion: A new method for the evaluation of layer potentials. *Journal of Computational Physics*, 252:332–349, November 2013.

[6] A. A. Kosterev, Yu A. Bakhirkin, R. F. Curl, and F. K. Tittel. Quartz-enhanced photoacoustic spectroscopy. *Optics Letters*, 27(21):1902–1904, November 2002.

[7] Anatoliy A. Kosterev and James H. Doty. Resonant optothermoacoustic detection: Technique for measuring weak optical absorption by gases and micro-objects. *Optics Letters*, 35(21):3571–3573, November 2010.

[8] Anatoliy A. Kosterev, Frank K. Tittel, Dmitry V. Serebryakov, Alexander L. Malinovsky, and Igor V. Morozov. Applications of quartz tuning

forks in spectroscopic gas sensing. *Review of Scientific Instruments*, 76(4):043105, March 2005.

[9] Rainer Kress. *Linear Integral Equations.* Springer Science & Business Media, Third edition, December 2012.

[10] Vladimir Maz'ya and Tatyana Shaposhnikova. Higher Regularity in the Layer Potential Theory for Lipschitz Domains. *Indiana University Mathematics Journal*, 54(1):99–142, 2005.

[11] Igor Moret. A Note on the Superlinear Convergence of GMRES. *SIAM Journal on Numerical Analysis*, 34(2):513–516, April 1997.

[12] P. Morse and K. Ingard. *Theoretical Acoustics.* Wed, 01/21/1987 - 12:00.

[13] Frank W. J. Olver, Daniel W. Lozier, Ronald F. Boisvert, and Charles W. Clark. *NIST Handbook of Mathematical Functions Hardback and CD-ROM.* Cambridge University Press, May 2010.

[14] Noemi Petra, John Zweck, Susan E. Minkoff, Anatoliy A. Kosterev, and James H. Doty. Modeling and Design Optimization of a Resonant Optothermoacoustic Trace Gas Sensor. *SIAM Journal on Applied Mathematics*, 71(1):309–332, January 2011.

[15] Manas Rachh, Andreas Klöckner, and Michael O'Neil. Fast algorithms for Quadrature by Expansion I: Globally valid expansions. *Journal of Computational Physics*, 345:706–731, September 2017.

[16] Youcef Saad and Martin H. Schultz. GMRES: A Generalized Minimal Residual Algorithm for Solving Nonsymmetric Linear Systems. *SIAM Journal on Scientific and Statistical Computing*, 7(3):856–869, July 1986.

[17] Artur K. Safin. *Modeling Trace Gas Sensors with the Coupled Pressure-Temperature Equations.* PhD thesis, December 2018.

[18] Matt Wala and Andreas Klöckner. A fast algorithm with error bounds for Quadrature by Expansion. *Journal of Computational Physics*, 374:135–162, December 2018.

[19] Matt Wala and Andreas Klöckner. A fast algorithm for Quadrature by Expansion in three dimensions. *Journal of Computational Physics*, 388:655–689, July 2019.

[20] Xiaoyu Wei, Shidong Jiang, Andreas Klöckner, and Xiao-Ping Wang. An integral equation method for the Cahn-Hilliard equation in the wetting problem. *Journal of Computational Physics*, 419:109521, October 2020.